Global transition zone tomography

Jeroen Ritsema[1] and Hendrik Jan van Heijst
Seismological Laboratory, California Institute of Technology, Pasadena, California, USA

John H. Woodhouse
Department of Earth Sciences, Oxford University, Oxford, UK

Received 3 June 2003; revised 21 August 2003; accepted 7 October 2003; published 3 February 2004.

[1] Our understanding of large-scale mantle dynamics depends on accurate models of seismic velocity variation in the upper mantle transition zone (400–1000 km depth). With the Mode Branch Stripping technique (MBS) of *van Heijst and Woodhouse* [1997] it is possible to extract the dispersion characteristics of overtone surface wave signals from single source-receiver overtone waveforms. Such data provide new global transition zone constraints. We combined more than a million measurements of path-average overtone phase velocity with normal-mode splitting functions and body wave travel times to construct model S20RTSb of shear velocity heterogeneity throughout the mantle. We discuss in detail the resolution of structural heterogeneity in the transition zone. The main observations are the following: (1) Large-scale shear velocity variations (15%) in the upper 250 km of the mantle are at least 5 times larger than deeper in the mantle. High-velocity keels of Archean cratons extend to about 200 km depth. Low velocities related to mid-ocean ridge upwelling are confined to the upper 150 km of the mantle. (2) The 220-km discontinuity in PREM cannot be reconciled with Rayleigh wave dispersion, especially in oceans. (3) The velocity below the oceanic lithosphere (350–400 km depth) is 1–1.5% lower than beneath the continental lithosphere. (4) High-velocity slabs of former oceanic lithosphere are conspicuous structures just above the 670-km discontinuity. They extend to about 1100 km depth in the South American, Indonesian, and Kermadec subduction zones, indicating that slabs penetrate through the 670-km phase transition in several subduction zones. (5) We observe lower-than-average shear velocity below the lithosphere at eight hot spots (including Hawaii, Iceland, Easter, and Afar). It is, however, difficult to accurately estimate their depth extent in the transition zone because of the limited vertical resolution. *INDEX TERMS:* 7218 Seismology: Lithosphere and upper mantle; 7255 Seismology: Surface waves and free oscillations; 7260 Seismology: Theory and modeling; 8120 Tectonophysics: Dynamics of lithosphere and mantle—general; 8180 Tectonophysics: Tomography;
KEYWORDS: tomography, surface waves, higher modes, transition zone, upper mantle

Citation: Ritsema, J., H. J. van Heijst, and J. H. Woodhouse (2004), Global transition zone tomography, *J. Geophys. Res.*, *109*, B02302, doi:10.1029/2003JB002610.

1. Introduction

[2] It is difficult to constrain the seismic structure of the transition zone between the upper and lower mantle (400–1000 km depth) because the two types of waves commonly used in global tomography are not particularly sensitive to velocity anomalies in this region of the mantle. Fundamental-mode surface waves, on the one hand, provide excellent global coverage of the uppermost mantle [e.g., *Trampert and Woodhouse*, 1995; *Laske and Masters*, 1996; *Zhang and Lay*, 1996; *Ekström et al.*, 1997], but they have limited sensitivity to seismic structure below 400 km depth. Teleseismic body waves, on the other hand, provide good sampling of the transition zone of subduction regions and beneath dense regional seismic networks, but global transition zone sampling is extremely heterogeneous [e.g., *Spakman*, 1990; *Fukao et al.*, 1992; *Grand*, 1994; *Vasco et al.*, 1994; *van der Hilst et al.*, 1997; *Boschi and Dziewonski*, 1999; R. Montelli et al., Global *P* and *PP* traveltime tomography: Rays versus waves, submitted to *Geophysical Journal International*, 2003, hereinafter referred to as Montelli et al., submitted manuscript, 2003]. Therefore models based on travel time or fundamental-mode surface wave data, or a combination of both, poorly constrain velocity heterogeneity between 300 and 1000 km depth (Figure 1). This makes it difficult to constrain structural heterogeneity in the transition zone and to determine whether or not there is material exchange between the upper and lower mantle.

[3] Surface wave overtones are, in principle, perfect complementary data for imaging the transition zone because they are sensitive to velocity variations well below 400 km depth,

[1]Now at Département de Sismologie, Institut de Physique du Globe, Paris, France.

0148-0227/04/2003JB002610$09.00

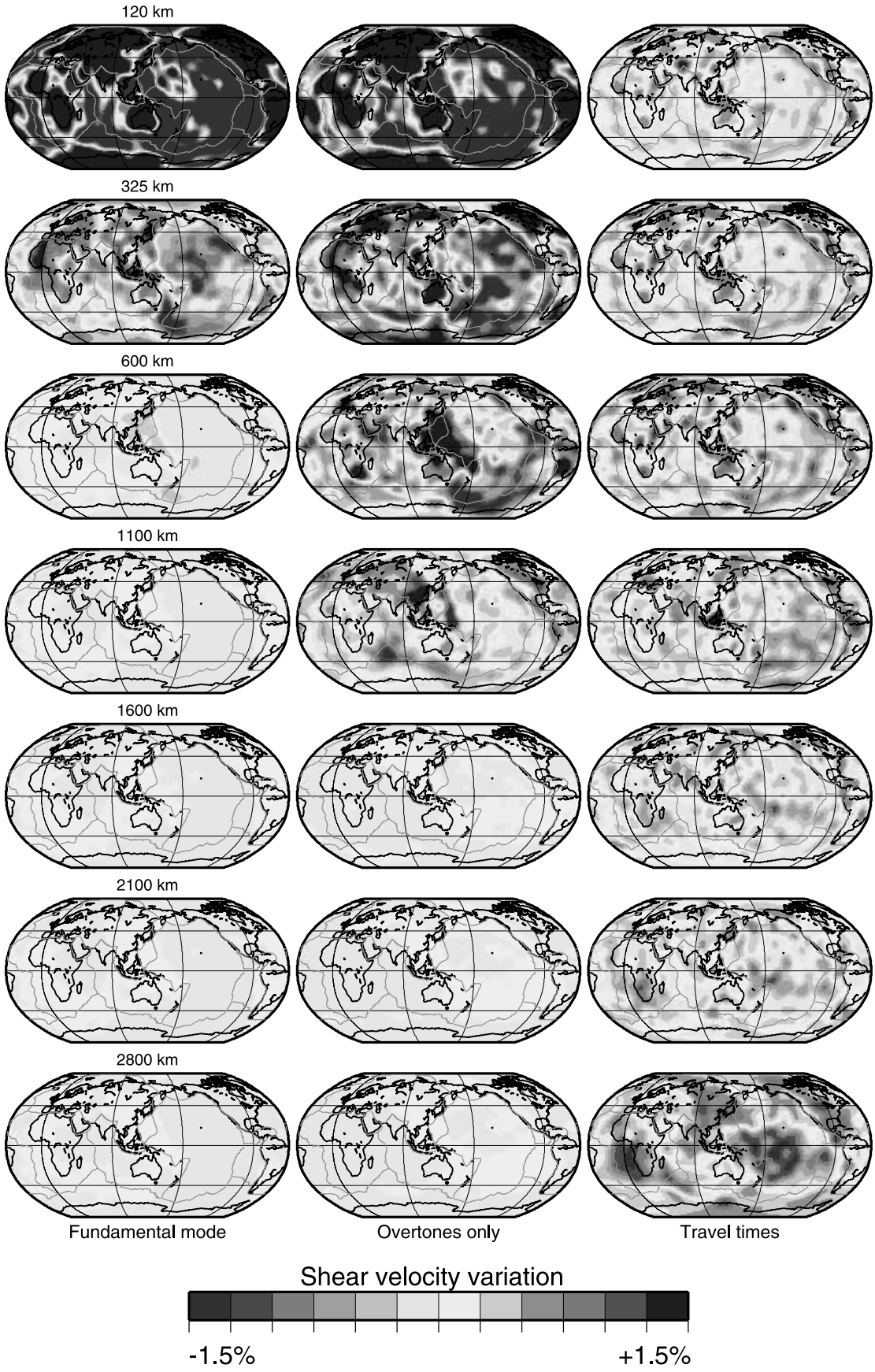
120 km
325 km
600 km
1100 km
1600 km
2100 km
2800 km
Fundamental mode
Overtones only
Travel times
Shear velocity variation
-1.5%
+1.5%

Figure 1.

and they provide better global transition zone sampling than body waves. Surface wave overtone waveforms are often included as direct constraints on mantle heterogeneity [*Woodhouse and Dziewonski*, 1984, 1986; *Tanimoto*, 1990; *Su et al.*, 1994; *Li and Romanowicz*, 1996; *Nolet*, 1990]. In global tomography, waveform techniques are applied to so-called "mantle waves" (predominantly long-period fundamental-mode surface waves) and long-period body wave waveforms. Typically, the body wave phases are modeled as a (coupled) superposition of dispersed surface wave modes or normal modes. However, waveform techniques do not involve extensive modeling of the low amplitude overtone signal, nor is it simple to assign weights to the different modal contributions to the waveform as constraints on mantle structure.

[4] Numerous studies have been devoted specifically to measure overtone dispersion [e.g., *Nolet*, 1975, 1977; *Mitchell*, 1980; *Cara*, 1978, 1979; *Okal and Jo*, 1987; *Stutzmann and Montagner*, 1993, 1994; *van Heijst and Woodhouse*, 1997; *Yoshizawa and Kennett*, 2002; *Beucler et al.*, 2003]. However, most of these techniques rely on either recordings from an array of seismometers [e.g., *Nolet*, 1975], or recordings of multiple earthquakes distributed over a wide depth range [e.g., *Stutzmann and Montagner*, 1993]. This severely restricts the number of paths for which overtone properties can be measured, and, hence, limits their applicability in global tomography.

[5] The Mode Branch Stripping technique of *van Heijst and Woodhouse* [1997] allows us to measure (path average) surface wave dispersion in single source-receiver recordings, which can be interpreted in the framework of surface wave ray theory. This technique is based on a waveform inversion technique introduced by *Lerner-Lam and Jordan* [1983, 1987] and expanded by others [*Cara and Lévêque*, 1987; *Debayle and Lévêque*, 1997]. *van Heijst and Woodhouse* [1999] (VHW99) demonstrated the accuracy of the MBS by comparing maps of fundamental as well as overtone surface waves.

[6] Previously, we presented model S20RTS of shear velocity in the mantle that was derived by inverting the Rayleigh wave phase velocity measurements of VHW99, together with teleseismic body wave travel time and normal-mode data [*Ritsema et al.*, 1999] (RHW99). In this paper we present a new version of model S20RTS, named S20RTSb, derived using the same model parameterization and inversion procedure, but with an expanded data set. We limit our discussion to structural heterogeneity in the transition zone, which is constrained primarily by our unique overtone Rayleigh wave data.

2. Data

[7] Model S20RTSb is based on three data types: normal-mode splitting, Rayleigh wave phase velocity, and body wave travel time. The normal-mode splitting data were measured by *Resovsky and Ritzwoller* [1999] and are the same data as used by RHW99. Both the phase velocity and travel time data sets are about a factor of 2 larger than the data sets used by RHW99.

Table 1. Number of Phase Velocity Measurements

	Minor Arcs		Major Arcs	
Branch	Period Range, s	Number of Measurements	Period Range, s	Number of Measurements
Fundamental mode	275–40	2,894,959	275–40	152,667
First overtone	235–40	255,932	200–69	44,678
Second overtone	114–40	243,458	131–62	41,339
Third overtone	88–43	236,592	69–51	30,694
Fourth overtone	62–40	230,362	56–46	46,965

[8] The phase velocity data set includes new measurements for earthquakes in 1996–2000. We have also analyzed radial component seismograms on which, in particular, the third and fourth overtone branches are optimally recorded. Our data set includes over 4 million Rayleigh wave phase constraints. Roughly a quarter of these phase velocity measurements are for overtones (Table 1).

[9] Following VHW99, we select high-quality data using "reliability threshold bands" which isolate measurements of high-amplitude overtone signals that are accurately reproduced by normal-mode synthetics. We reject from these data phase velocity measurements that do not fit smooth phase velocity maps, and we exclude Rayleigh wave modes with fewer than 1000 reliable phase velocity measurements. Data coverage is best for the fundamental-mode Rayleigh wave, which is recorded with highest amplitude and is isolated from the overtones (Figure 2).

[10] The body wave data set includes new travel time measurements for events from 1998 to 2001. The measurements are made by cross-correlating low-pass-filtered ($T >$ 16 s) transverse component seismograms with normal-mode synthetics for the Preliminary Reference Earth Model (PREM) [*Dziewonski and Anderson*, 1981] seismic velocity structure and Harvard centroid moment tensor (CMT) source parameters. We discard seismograms with low signal-to-noise ratios and which exhibit high-amplitude coda nor do we measure the travel time of a body wave that arrives within 40 s of another major body wave phase. Furthermore, we require that A_1 and A_2, which minimize

$$\int_w [d(t) - A_1 s(\tau_m - t)]^2 \, dt$$

and

$$\int_w \left[A_2^{-1} d(t) - s(\tau_m - t)\right]^2 \, dt,$$

Figure 1. Models of shear velocity derived by inverting (left) fundamental-mode Rayleigh wave phase velocities (40–200 s), (middle) overtone Rayleigh wave phase velocities, and (right) teleseismic body wave travel times. The color intensity is proportional to the amplitude of the shear velocity perturbation. The color scale ranges from −1.5% to +1.5% to facilitate a comparison of the maps, but actual velocity variations in the uppermost mantle are higher. Velocity heterogeneity can be resolved to at most 400 km depth with fundamental mode Rayleigh wave data, while teleseismic body wave travel times cannot constrain vertical velocity variations in the upper 1000 km of the mantle. Overtone data ideally complement fundamental-mode Rayleigh wave and travel time data for constraining structure in the transition zone. See color version of this figure at back of this issue.

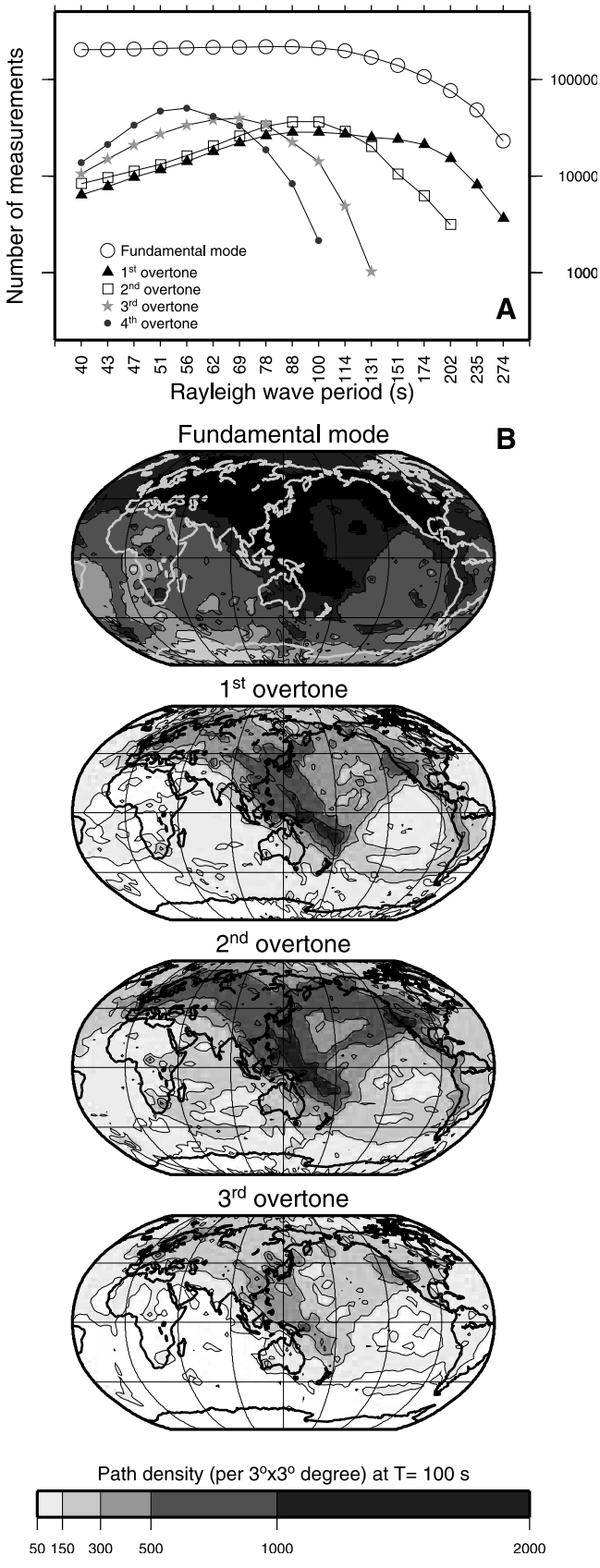

Figure 2.

Table 2. Number of Travel Time Measurements

Phase	Number of Measurements	Variance Reductions, %	Average Delay, s	Average Residual Delay, s
S, S_{diff}	46,933	71	4.02	1.91
SS	33,203	77	5.03	2.15
SSS	7,409	77	6.55	2.85
SKS	13,560	57	3.00	1.81
$SKKS$	6,356	47	2.80	1.97
ScS	4,298	67	3.79	1.95
ScS_2, ScS_3	2,784	75	5.63	2.65

agree to within a factor of 1.1. When $A_1 \approx A_2$, body wave signals have low-amplitude coda and wave shapes that are similar to those in one-dimensional (1-D) synthetics and their travel times can be measured most precisely. The data sets includes a total of 115,000 absolute travel time delays (Table 2) with measurement errors of, at most, 1 s.

3. Modeling Approach

3.1. Theoretical Simplifications

[11] We relate a phase velocity anomaly $\delta c(\omega)$ to shear velocity heterogeneity $\delta V_s(\mathbf{x})$ in a linear fashion under the assumption that the Rayleigh wave is affected by seismic structure in the mantle beneath the great circle arc L (with length Δ) and that we can employ sensitivity kernels $\partial c_n(\omega)/\partial V_0(r)$, computed for a 1-D reference model (Figure 3):

$$\delta c(\omega, n) = \frac{1}{\Delta} \int_L d\mathrm{l} \int d\mathrm{r} \left(\frac{\partial c_n(\omega)}{\partial V_0(r)} \right) \delta V_s(\mathbf{x}). \tag{1}$$

Although several researchers report that fundamental-mode surface waves may propagate off the great circle [e.g., *Lay and Kanamori*, 1985; *Woodhouse and Wong*, 1986; *Pollitz*, 1994; *Wang et al.*, 1998], we expect the "great circle approximation" to be sufficiently accurate for higher-mode Rayleigh waves since they are primarily sensitive to the deeper parts of the upper mantle where velocity heterogeneity is relatively small.

[12] Travel times are modeled under the assumption that the body wave is sensitive to structure along the ray path S^0, which is computed for the PREM model:

$$\delta T = - \int_{S^0} \frac{\delta V(\mathbf{r})}{V_0^2(\mathbf{r})} \, ds. \tag{2}$$

Since we are ignoring the effects of wave front healing in body wave propagation, it is likely that we are under-

Figure 2. (a) Number of phase velocity measurements of the fundamental-mode (open circle), and the first (triangle), second (square), third (star), and fourth (solid circle) overtone Rayleigh wave between 40 and 274 s period used in this study. (b) Path density (number of paths per $3^\circ \times 3^\circ$ area) of the (from top to bottom) fundamental-mode, first, second, and third higher-mode Rayleigh wave with a period of 100 s. Note that the higher-mode path density is in most regions at least 50, though it is relatively low in, particularly, the Southern Hemisphere. The difference between fundamental-mode and overtone path coverage is the same for other periods.

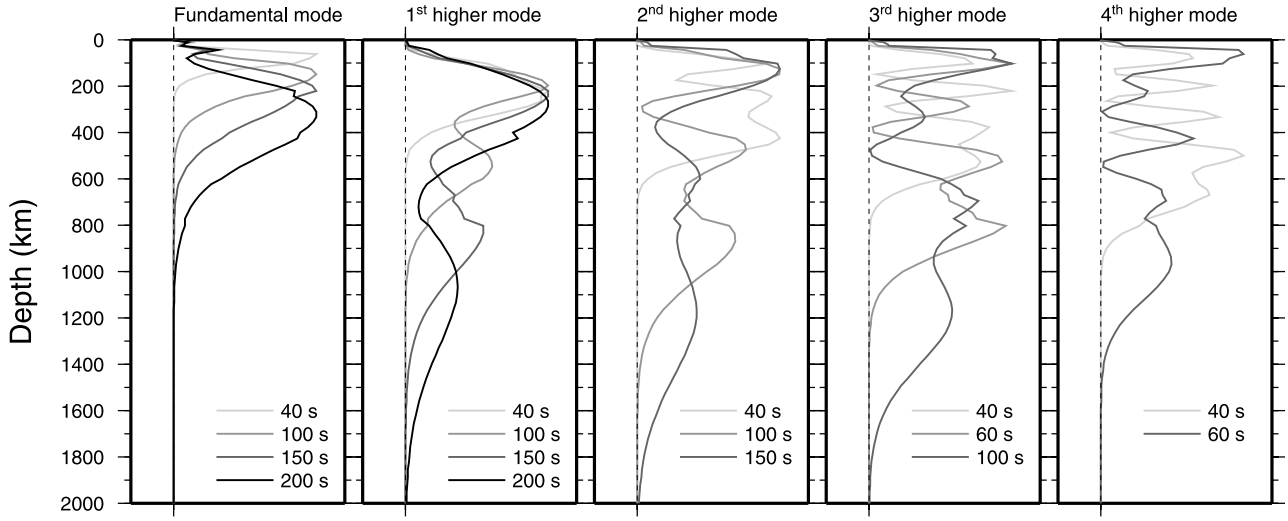

Figure 3. Sensitivity kernels (normalized so that they have a maximum amplitude of 1) ($\partial c(\omega)/\partial V_s^0(r)$) which relate phase velocities of the fundamental (left) and the first, second, third, and fourth overtone Rayleigh waves to shear velocity $V_0(r)$ for the PREM model.

estimating the amplitude of δV_s in the lower mantle, in particular at the shortest scale lengths [e.g., *Li and Romanowicz*, 1995; *Nolet and Dahen*, 2000; Montelli et al., submitted manuscript, 2003].

3.2. Model Parameterization

[13] We parameterize the model of shear velocity perturbations $\delta V_s(\mathbf{x})$ from the PREM model using 21 spline functions (Figure 4) and spherical harmonic basis functions up to degree and order 20:

$$\delta V_s(\mathbf{x}) = \sum_{k=1}^{21} \sum_{l=0}^{20} \sum_{m=-l}^{l} m_{klm}\, z_k(r) Y_l^m(\theta, \phi), \qquad (3)$$

where $z_k(r)$ represent the splines as a function of depth and $Y_l^m(\theta, \phi)$ is the spherical harmonics.

[14] The spline functions provide continuous parameterization across the 670-km discontinuity. The spacing of the splines is smallest in the uppermost mantle to allow for the highest vertical resolution at shallow depths where the resolving power of the data is highest.

3.3. Model Simplifications

[15] We simplify the model in several aspects. First, we restrict the modeling to isotropic shear velocity anomalies with respect to the (anisotropic) PREM model, which contribute most to the observed phase velocity anomalies. We refer to *Montagner* [1998], *Ekström and Dziewonski* [1998], *Trampert and van Heijst* [2002], and *Gung et al.* [2003] for recent studies of upper mantle seismic anisotropy. Second, we account for the contribution of *P* velocity anomalies to the Rayleigh wave phase anomalies, assuming that *P* velocity anomalies are related to *S* velocity anomalies throughout the mantle by $2d\ln V_p = d\ln V_s$. This scaling is based on globally recorded *P* and *S* wave travel time residuals [e.g., *Souriau and Woodhouse*, 1985; *Robertson and Woodhouse*, 1995; *Bolton and Masters*, 2001]. This ratio is not accurate for all velocity anomalies in the mantle. For example, *Ritsema and van Heijst* [2001] and *Antolik et*

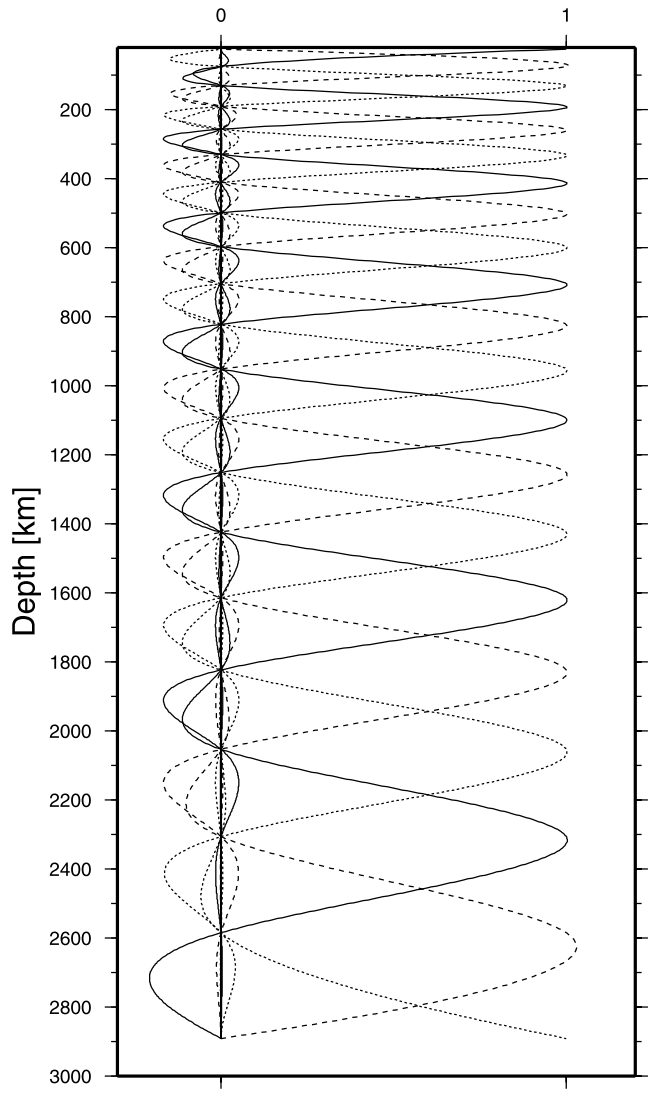

Figure 4. Spline functions used to parameterize the depth dependence of shear velocity heterogeneity.

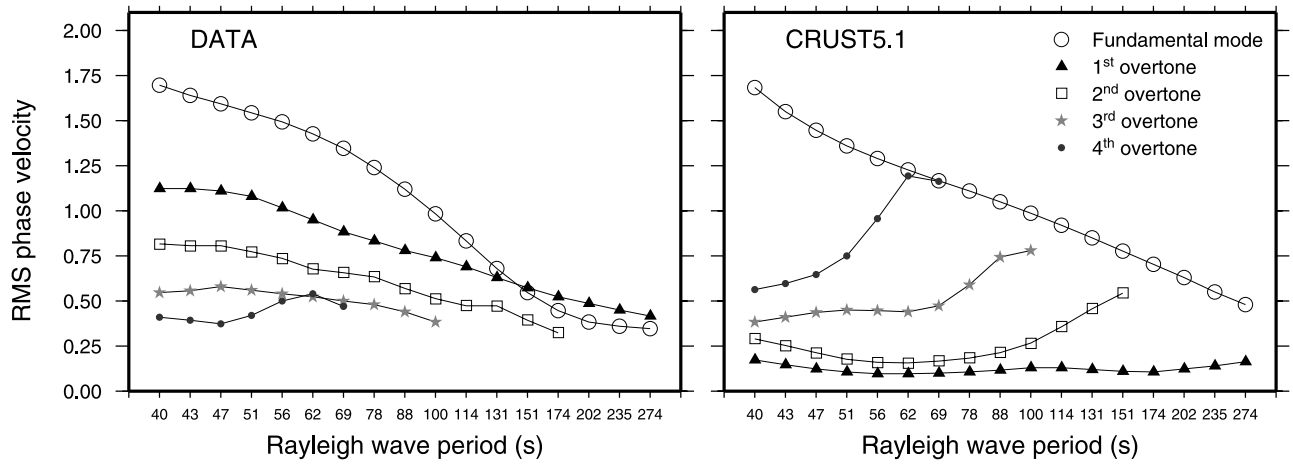

Figure 5. Root-mean-square (RMS) phase velocity perturbation from PREM (in percent) of the fundamental-mode (open circle), and the first (triangle), second (square), third (star), and fourth (solid circle) overtone Rayleigh wave phase velocity (left) seen in the data and (right) due to crustal thickness and velocity variations in model CRUST5.1 [*Mooney et al.*, 1998].

al. [2003] show that the *P* velocity in the uppermost mantle beneath oceans is lower than predicted by a scaled *S* velocity model. However, we expect the effects of inhomogeneous scaling on the velocity models to be small as the sensitivity to *S* velocity is dominant for most modes considered. Third, we do not consider perturbations to the depth of seismic discontinuities incorporated in the PREM model. Undulations of the 410-km and 670-km discontinuities have been reported by many researchers [e.g., *Shearer*, 1990; *Shearer and Masters*, 1992; *Estabrook and Kind*, 1996], but their effect on the resolution of shear velocity heterogeneity appears to be minor [*Gu et al.*, 2003].

3.4. Crustal Corrections and Earthquake Relocations

[16] Figure 5 demonstrates that the effects of the crust on Rayleigh wave propagation are significant. For the fundamental-mode Rayleigh wave and the highest overtones, the RMS of the phase velocity distribution due to CRUST5.1 and the RMS derived from the data have similar amplitudes. The RMS of the crustal corrections is small compared to the observed RMS for the first and second Rayleigh overtone indicating that these overtones provide constraints on mantle structure that are largely independent of the crust. The strongest signal that the crust imparts on the Rayleigh wave dispersion is due to differences in the crustal structure of oceans and continents structure which are, to first order, well understood.

[17] We remove the effects of the crust by using model CRUST5.1 of *Mooney et al.* [1998] as a priori model of the crust. This model defines the crustal *P* and *S* velocity and density as a function of depth in $5^\circ \times 5^\circ$ cells. To determine the crustal correction for the phase velocity measurements, we superimpose CRUST5.1 on PREM and calculate local eigenfrequencies for the modes used in the modeling in each cell. We expand the gridded local eigenfrequency perturbations with respect to PREM in spherical harmonics and subtract the contribution of CRUST5.1 from each individual measurement.

[18] In addition to crustal travel time contributions, we subtract systematic contributions to the travel time anomalies that can be explained by earthquake (point source) mislocations and origin time errors in the Harvard CMT catalog. We determine the preferred earthquake locations and origin times by fitting observed travel times to predictions for a smooth degree-12 velocity model that is derived from the splitting and phase velocity data, and from differential body wave travel times (e.g., $S - SS$, $S - SKS$, $S - SKKS$, $ScS - S$). These data types are insensitive to uncertain earthquake locations and origin times.

3.5. Inversion and Damping

[19] To assign appropriate weights to the fundamental and overtone Rayleigh wave modes, we apply weights to each mode according to the a posteriori estimate of the average standard deviation in the phase velocity measurements. We estimate the standard deviations for each mode from smooth phase velocity maps. The travel time measurements are given equal weight.

[20] To regularize the mixed determined inverse problem, we apply model norm damping. We prefer this over smoothness constraints because of the inhomogeneous distribution of the data and because smoothness constraints suppress strong lateral and vertical velocity gradients at, for instance, continental margins and within subduction zones. The damped least squares solution $\mathbf{m}$ is given by

$$\mathbf{m} = \left(A^T A + \epsilon I\right)^{-1} A^T \mathbf{d}. \tag{4}$$

We construct the inner product matrix of the data derivatives $A^T A$ and use eigenvalue decomposition to invert it. We choose ϵ so that the model $\mathbf{m}$ is composed of about 3000 effective unknowns (i.e., the trace of the resolution matrix is equal to 3000).

3.6. Model Resolution

[21] A Backus-Gilbert averaging kernel $R(\mathbf{x}, \mathbf{x}_0)$ is defined by

$$m(\mathbf{x}_0) = \int_V dV\ R(\mathbf{x}, \mathbf{x}_0)\ e(\mathbf{x}) \tag{5}$$

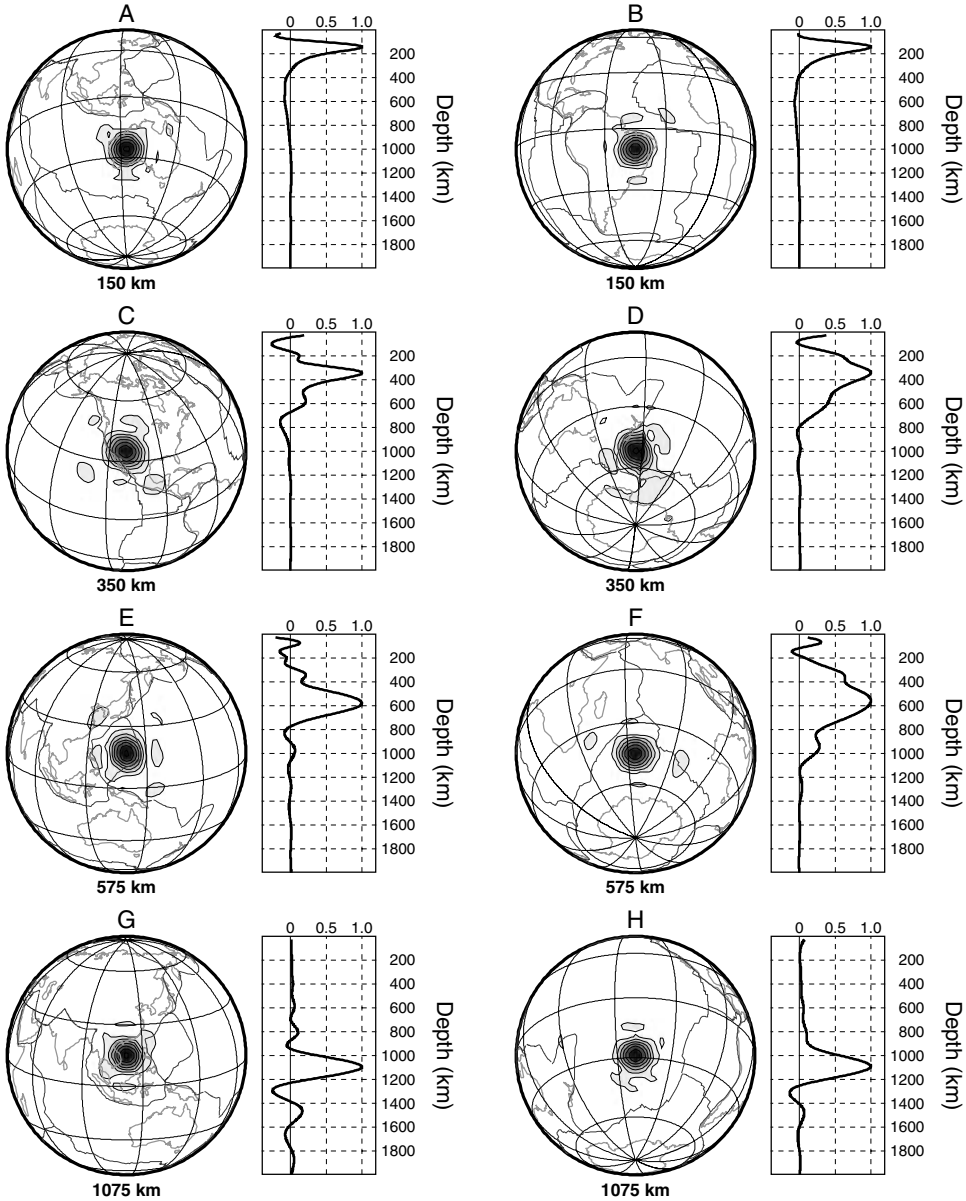

Figure 6. Backus-Gilbert resolution kernels for points beneath (a) Australia (150 km), (b) Brazil (150 km), (c) western United States (350 km), (d) southwest Pacific (350 km), (e) Mariana Islands (575 km), (f) Indian Ocean (575 km), (g) southeast Asia (1075 km), and (h) southern Pacific (1075 km). Map views of the Backus-Gilbert kernels are shown on the left. The radial dependence of the kernels is shown on the right.

and describes how the value obtained in the generalized model $m(\mathbf{x}_0)$ at $\mathbf{x}_0$ is a spatial average over the true structure $e(\mathbf{x})$ [*Backus and Gilbert*, 1968]. Ideally, these kernels are delta functions in space, but given finiteness of model parameterization, incomplete data coverage, and the damping applied in inversion these kernels have a finite spatial extent.

[22] Figure 6 shows horizontal and vertical cross sections through Backus-Gilbert kernels computed for eight locations in the mantle to illustrate the variable model resolution in S20RTSb. Velocity heterogeneity in the upper 200 km of the mantle is resolved with highest resolution (Figures 6a and 6b). Heterogeneity in this region is constrained primarily by fundamental mode Rayleigh wave that provide nearly homogeneous global coverage. Vertical resolution strongly varies in the transition zone because overtone data coverage varies strongly (Figure 2). In the western Pacific, eastern Asia, and North America, where overtone data coverage is best, shear velocity heterogeneity at 300 km depth is independently resolved from that at 650 km depth (e.g., Figures 6c and 6e), while in, for example, the Southern Hemisphere shear velocity heterogeneity at 350–600 km depth represents a (weighted) vertical average of heterogeneity over a 500-km depth range (Figures 6d and 6f). Teleseismic body waves, especially *SS*, help to improve resolution in the deepest parts of the transition zone where their sampling density is highest.

[23] Backus-Gilbert kernels are useful for determining whether or not anomalies in S20RTSb are artifacts. For

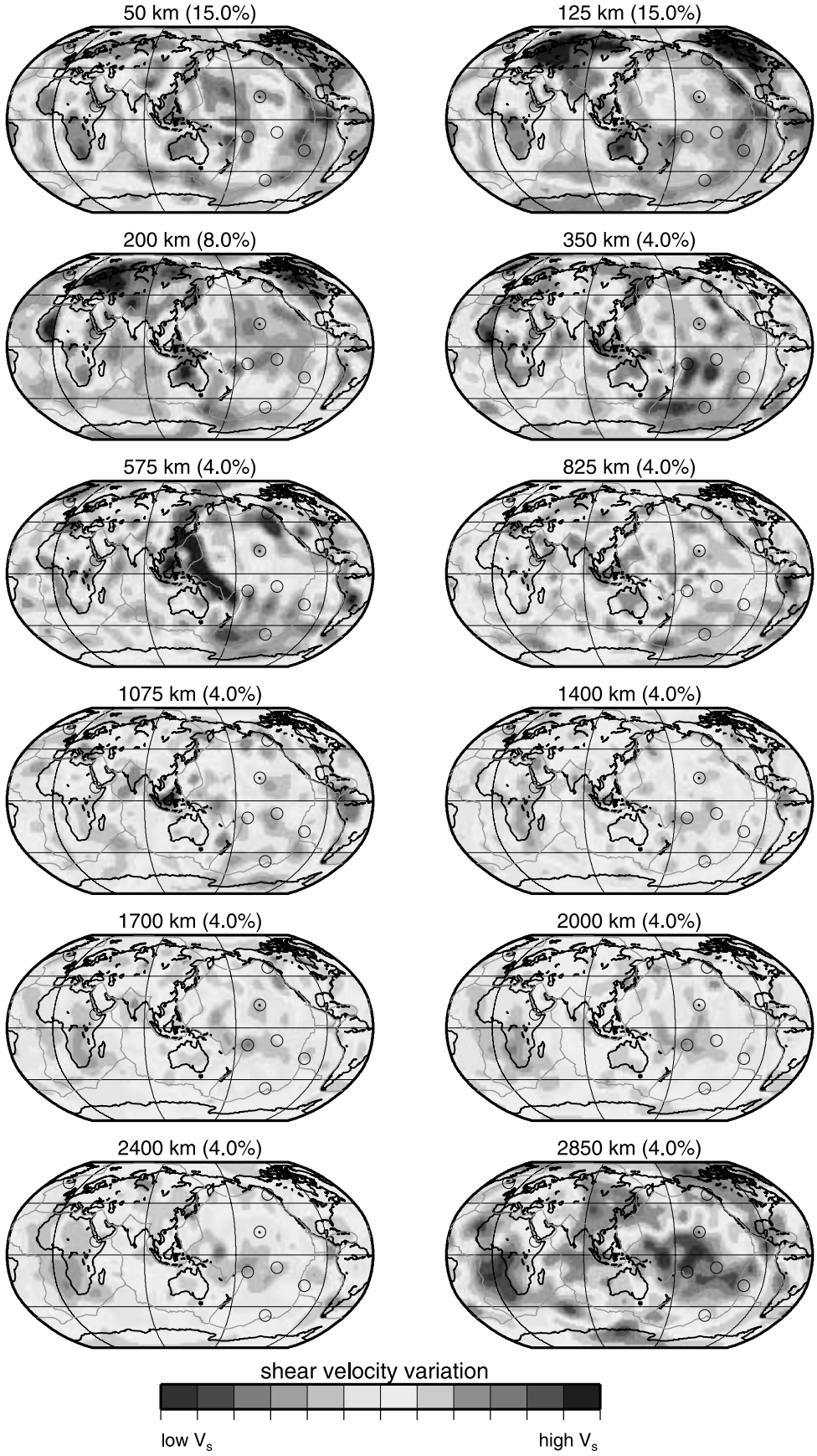
50 km (15.0%)
125 km (15.0%)
200 km (8.0%)
350 km (4.0%)
575 km (4.0%)
825 km (4.0%)
1075 km (4.0%)
1400 km (4.0%)
1700 km (4.0%)
2000 km (4.0%)
2400 km (4.0%)
2850 km (4.0%)
shear velocity variation
low V_s
high V_s

Figure 7.

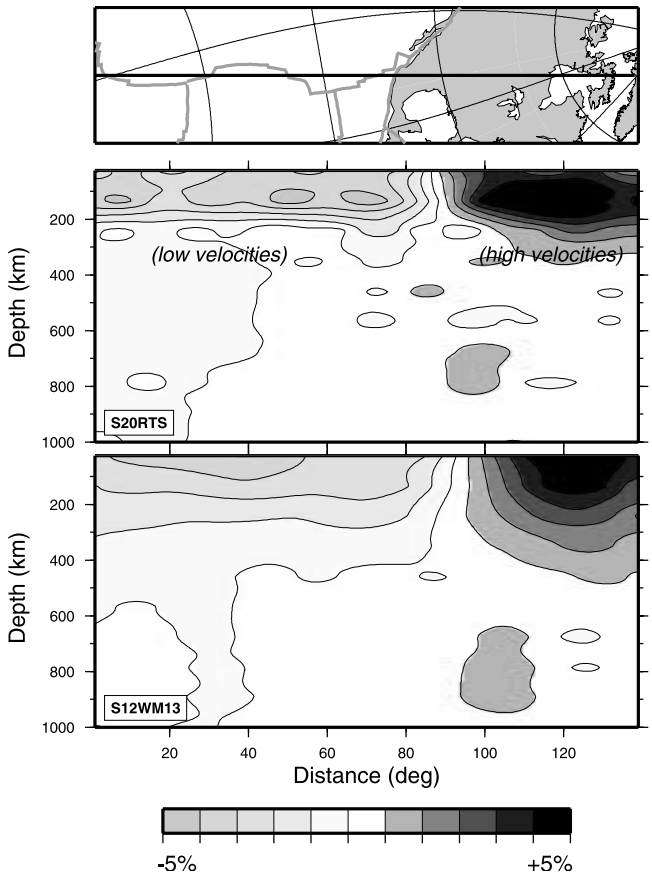

Figure 8. (top) Vertical cross section through (bottom) models S20RTSb and S12WM13 beneath a great circle path along the East Pacific Rise (EPR) (where shear velocities are relatively low), and the North American continent (where shear velocities are relatively high).

example, the high δV_s anomaly at 1075 km depth beneath Indonesia is not a result of "vertical smearing" of higher-velocity structure in shallower regions of the upper mantle. The Backus-Gilbert kernel computed for a depth of 1075 km has an amplitude lower than 0.1 at depths shallower than 800 km which indicates that the high velocity at 1075 km is independently constrained. On the other hand, the vertical extent of the velocity anomaly at 350 km depth south of New Zealand (Figure 6d) and at 575 km depth beneath Kerguelen Island (Figure 6f) is uncertain, given the broad depth extent of the resolution kernels.

4. The 3-D Model S20RTSb

[24] In Figure 7 we present 12 maps of δV_s according to model S20RTSb. Model S20RTSb features the major tectonic and geologic structures in the upper 200 km of the mantle that are present in all tomographic models based on surface wave data. These include low δV_s structures in the upper 50–100 km beneath mid-ocean ridges, the East African Rift region, and convergent margins, high δV_s structures beneath continental shields, and the systematic increase of shear velocity with increasing plate age. However, compared to "older" models such as S12WM13 [*Su et al.*, 1994], the lateral and depth resolution of δV_s is greatly enhanced (Figure 8). The stronger vertical gradients of δV_s show that there is not a clear seismic signature of the continental keels and mid-ocean ridge upwellings below 200–250 km depth.

[25] Beneath oceans, a high shear velocity lid with a thickness of approximately 100 km overlies the asthenosphere with relatively low shear velocities. At >350 km depth the heterogeneity is dominated by the subduction of former oceanic lithosphere. The fact that the elongated high-velocity slabs at 575 km depth are not seen at 825 km depth indicates that the 660-km phase transition impedes the descent of slabs in agreement with the conclusions of [*Gu et al.*, 2001a].

[26] It is not obvious that convection in the mantle above the 660-km discontinuity is completely decoupled from that below it, an assertion that has recently been reviewed by *Hamilton* [2002]. There are continuous high-velocity anomalies through the 660-km discontinuity to at least 1100 km depth beneath northern South America, Indonesia, and Kermadec that cannot be dismissed as modeling artifacts (i.e., "vertical smearing"). *Cizkova et al.* [1999] speculate that continuity of high-velocity anomalies in the lower mantle can be caused by thermal coupling across an impermeable boundary. The drop in the amplitude of δV_s across the 660-km discontinuity may provide useful constraints on physical parameters (e.g., viscosity structure, thermal diffusivity) to make such a mechanism plausible.

[27] There are also velocity anomalies in the transition zone that are not fully understood. A low δV_s anomaly in the northeastern Pacific may be the same anomaly as the low-velocity anomaly beneath the Bowie hot spot inferred by *Nataf and VanDecar* [1993] observed in body wave travel time variations across the Washington Regional Seismic Network albeit that this anomaly is more extensive in S20RTSb.

[28] A low-velocity anomaly in the southwest Pacific stronger and broader than low shear velocities beneath the "central Pacific hot spot group" and it correlates with widespread magmatism in the region. This anomaly has also been noted in surface wave group velocity tomography [*Ritzwoller et al.*, 2001]. Preliminary models suggest a relation to the detachment of dense slabs in the Eocene, and the rise of warmer mantle material in surrounding regions (C. Finn, personal communication, 2003).

[29] The shear velocity between 300 and 700 km beneath the central Atlantic Ocean is higher than beneath other oceanic basins for the same depth range (Figure 9). This

Figure 7. Maps of shear velocity variation according to model S20RTSb at 50, 125, 200, 325, 575, 825, 1075, 1400, 1700, 2000, 2400, and 2850 km depth. The shear velocity is higher (lower) than the shear velocity in PREM in blue (red) regions. The color intensity is proportional to the amplitude of the shear velocity perturbation. The peak shear velocity perturbation from PREM (in percent) is given above each map. Green lines represent plate boundaries, while the blue circles are at the locations of the Afar, Iceland, Hawaii, Samoa, Tahiti, Easter Island, McDonald, and Bowie hot spots. See color version of this figure at back of this issue.

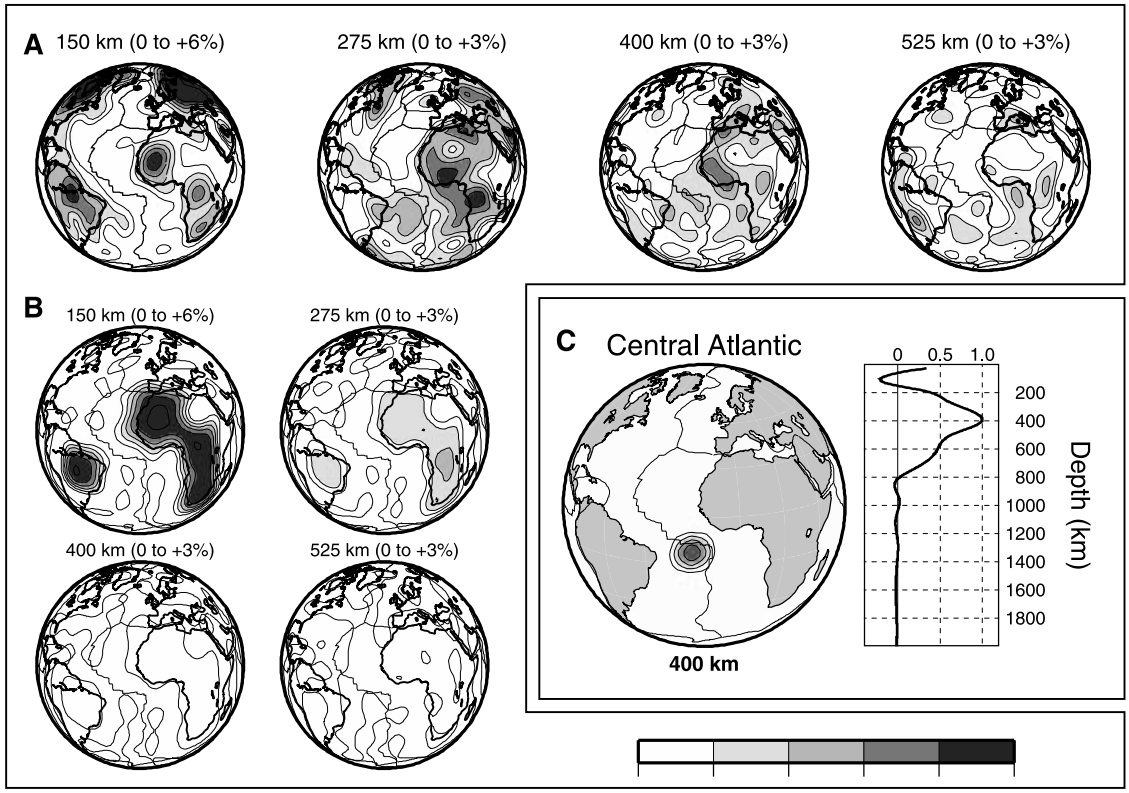

Figure 9. (a) Maps of shear velocity variations in the upper mantle beneath the central Atlantic. The depth and peak shear velocity perturbation from PREM (in percent) are given above each map. (b) Resolution test showing how the mantle would be imaged with the data and the inversion procedure used in this study if 200-km-thick high-velocity (6% higher than in the PREM) structures beneath the cratons in South America and Africa are the only anomalies present in the mantle. (c) Backus-Gilbert resolution kernel demonstrating further that the high-velocity anomaly seen at 400 km depth beneath the central Atlantic is independently resolved nearby high-velocity cratons. The depth extent of the anomaly is poorly constrained.

high-velocity anomaly may be related to what *Bonatti* [1996] calls the "equatorial Atlantic thermal minimum" seen geophysically as a region with long transform faults, high gravity, anomalous ocean depth, and low melt production. It is the region of the Atlantic that formed during the final stages of the opening of the Atlantic because it was presumably the strongest part of the Pangean continent. The anomaly is at >200 km depth, but depth resolution is too poor to constrain its depth extent in the upper mantle.

[30] *King and Ritsema* [2000] speculated that the high shear velocity anomaly, that appears particular obvious as an elongated structure along the Atlantic coast of Africa is a signature of the downwelling in "edge-driven convection" triggered by the contrast in rheology of oceanic lithosphere and the thick West African and Congo cratons.

4.1. Radial Profiles of δV_s

[31] Figure 10 shows depth profiles of δV_s to illustrate the difference in upper mantle structure beneath continental shields and oceans. Figure 10a illustrates that the high-velocity anomalies beneath cratons are confined to the upper 250–300 km of the mantle, although the maximum amplitude of the δV_s perturbation varies between locations. The base of the cratonic lithosphere, defined as the depth where the (negative) δV_s gradient is largest, ranges from 175 to 230 km. These differences are for the most part due to the slight differences in model resolution.

[32] Figure 10b shows that δV_s beneath mid-ocean ridges peaks at about 100 km depth. As shown before, the shear velocity is lowest beneath the East Pacific Rise, the fastest spreading ridge on Earth. All ridges have in common that below about 200 km depth δV_s is similar to δV_s determined for the Oceanic Reference Model, which represents "normal" oceanic mantle. that features a low-velocity asthenosphere to about 350 km depth.

[33] While the strongest shear velocity contrast between oceanic and continental mantle is situated in the upper 200 km of the mantle, there is a 1% velocity contrast between the continental and oceanic mantle to at least 350 km depth (Figure 10c). The globally average δV_s (the "$l = 0$" term in equation (3)), as well as the average δV_s for oceans oscillate between the 100 and 300 km depth. This complexity is a result of the 220-km discontinuity in PREM that cannot be reconciled with Rayleigh wave dispersion data, especially for oceanic paths. This agrees with the absence of body wave reflections from a depth of 220 km in global stacks [*Shearer*, 1990, 1993] and the suggestion that the 220-km discontinuity exists beneath continents only [e.g., *Gu et al.*, 2001b; *Deuss and Woodhouse*, 2002]. Of course, the 220-km discontinuity can only be modified slightly in the inversion process

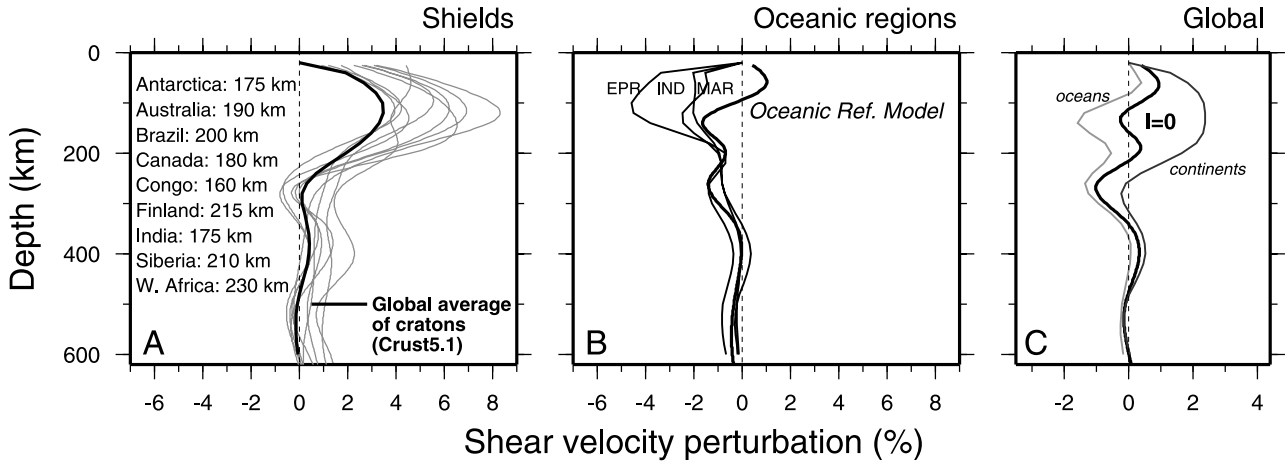

Figure 10. (a) Profiles of δV_s as a function of depth beneath nine locations in worldwide shields. (b) Profiles of (thin lines) the average δV_s beneath the East Pacific Rise, the Indian Rise, the Mid-Atlantic Ridge, and (thick line) beneath oceans that are between 5500 and 6500 m deep and have a crust that is between 40 and 80 Myr old. We refer to this profile as the Oceanic Reference Model. (c) Profiles of (thin lines) the average δV_s beneath oceans and continents and (thick line) the global average δV_s (labeled 'l = 0'). The dashed line in Figures 10a, 10b, and 10c represents PREM.

because of the smooth parameterization and the model norm damping.

4.2. Amplitude Spectrum

[34] Figure 11 shows the spectral amplitude of S20RTSb for the depths corresponding to the maps shown in Figure 7. At depths smaller than 150 km, the lower harmonic degrees contain significantly more power than at the higher degrees. However, in contrast to the suggestion by *Su and Dziewonski* [1991] the power spectrum does not fall off rapidly beyond degree 12, indicating that the dominance of long-wavelength structures is limited to the lowest degrees

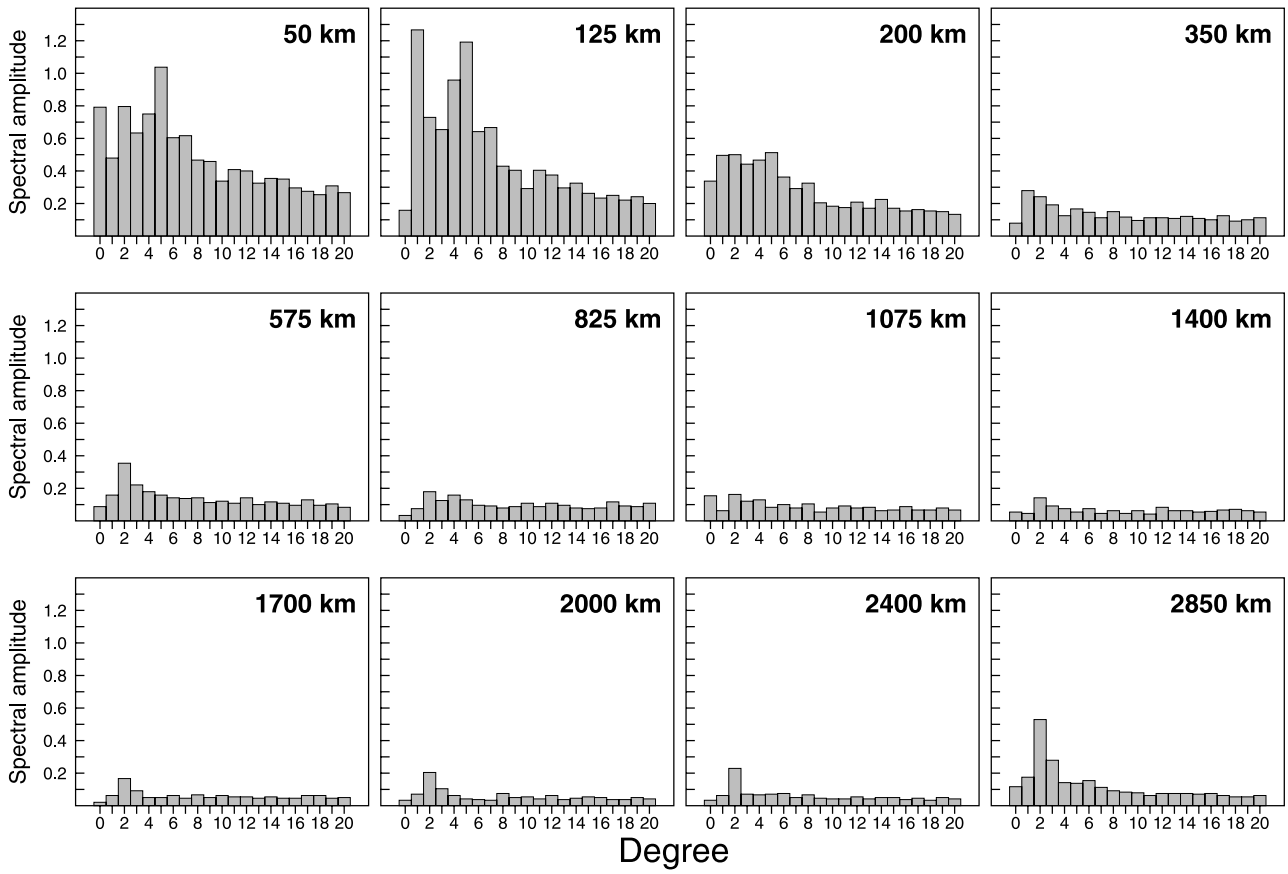

Figure 11. S20RTSb spectral amplitudes as a function of harmonic degree l for depths at which the model is plotted in Figure 7.

Table 3. Variance Reduction of Rayleigh Wave Phase Velocity Measurements

		Minor Arcs		Major Arcs	
Mode	Period, s	S20RTSb	Maps	S20RTSb	Maps
Fundamental mode	150	68	67	76	75
	100	86	85	90	89
	40	91	92	87	90
First overtone	150	66	73	49	60
	100	82	86	68	73
	56	82	90	–	–
Second overtone	114	51	60	54	65
	69	83	86	64	69
Third overtone	78	62	73	46	78
	56	73	78	55	70
Fourth overtone	56	75	79	50	55
	46	56	63	–	–

and probably associated with the distribution of oceans and continents. Because of the theoretical simplifications it is possible to constrain only the large-scale velocity variations in the mantle. Tomographic models do not adequately account for relatively short-wavelength (<1000 km) heterogeneity, abrupt lateral changes in lithospheric thickness [e.g., *Melbourne and Helmberger*, 2001] and sharp sides of deep mantle structures [e.g., *Ritsema et al.*, 1998; *Ni et al.*, 2002] that are obvious in regional network recordings.

5. Concluding Remarks

[35] Model S20RTSb unique combination of overtone Rayleigh wave data that ideally complement teleseismic travel time. The independent measurement of overtone phase velocities using the mode branch stripping technique and the subsequent inversion for seismic structure allows the low-amplitude overtone signals to be used. Because we include overtones up to the fifth branch, structures to depths as great as 1000 km are constrained by both surface wave dispersion data and surface reflected body waves (e.g., *SS*).

[36] In Table 3, we show the variance reductions for representative modes achieved with S20RTSb and with smooth phase velocity maps with approximately 150 effective unknowns (see VHW99). For most modes, the variance reductions achieved with S20RTSb are only slightly lower than the variance reductions achieved with the phase velocity maps. This demonstrates that the independently measured phase velocity anomalies for the different mode branches are, to a large degree, reconciled by S20RTSb. Hence the major modeling assumptions such as the "great circle propagation," the linearized sensitivity of phase velocity to mantle structure, the neglect of variable anisotropy and the scaling of *P* and *S* velocities appear to be good to first order.

[37] In Figure 12, we compare S20RTSb with four other global shear velocity models:

[38] 1. The S20A_SV [*Ekström and Dziewonski*, 1998] model is constrained by fundamental-mode Rayleigh wave phase velocity data, body wave travel times and overtone waveform data.

[39] 2. The SB4L18 [*Masters et al.*, 2000] model is constrained by Rayleigh and Love wave phase velocities,

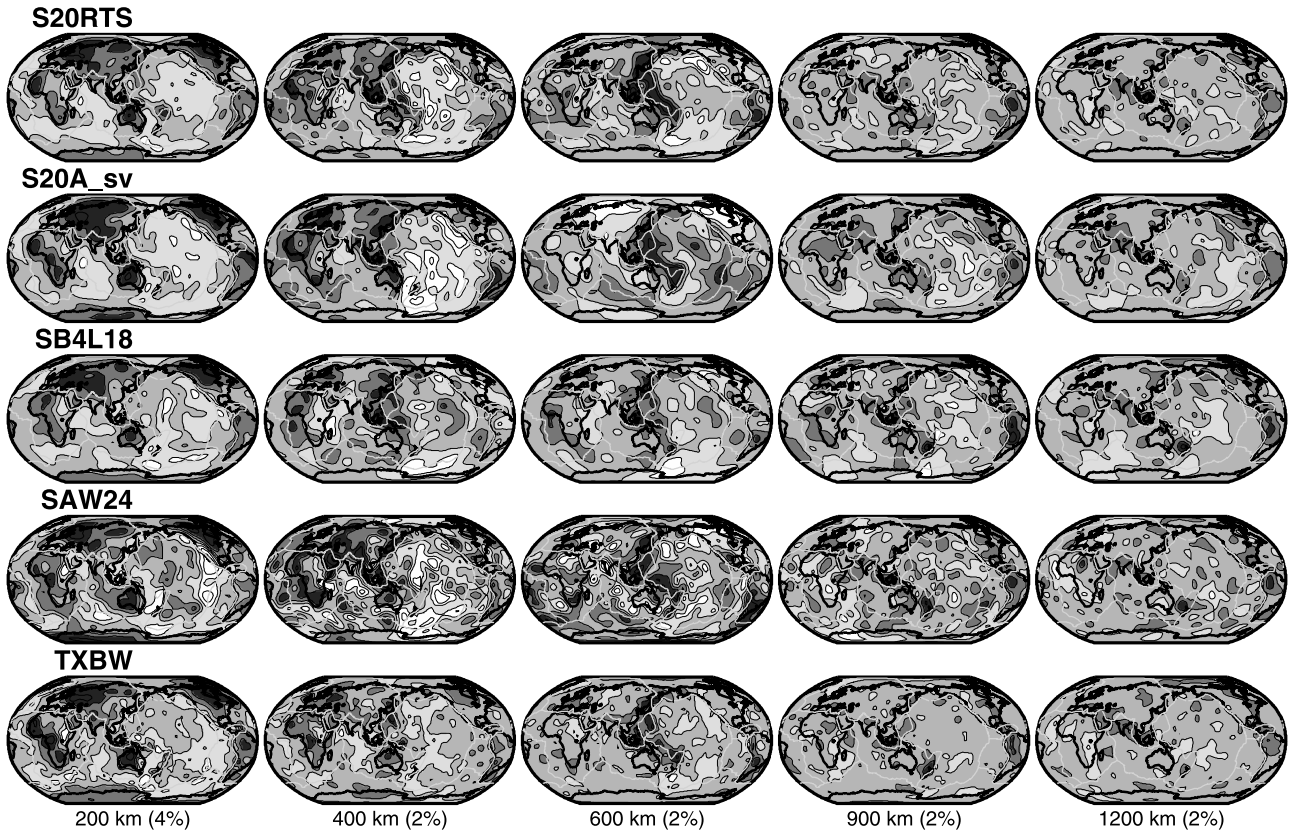

Figure 12. Comparison of models S20RTSb (this study), S20A_SV [*Ekström and Dziewonski*, 1998], S12WM13 [*Su et al.*, 1994], SAW24 [*Mégnin and Romanowicz*, 2000], and TXBW [*Grand*, 2002] at 200, 400, 600, 900, and 1200 km depth.

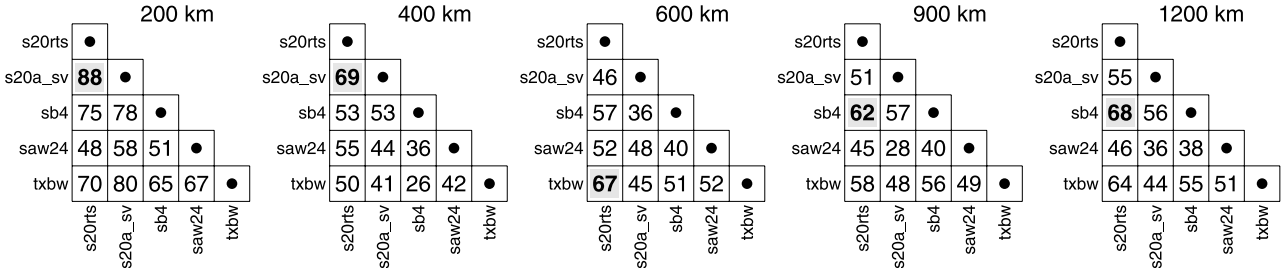

Figure 13. Model correlation, determined by the inner products of the model vectors up to degree 20, of the models shown in Figure 12 at 200, 400, 600, 900, and 1200 km depth.

free-oscillation structure coefficients, and body wave travel times.

[40] 3. The SAW24 [*Mégnin and Romanowicz*, 2000] model is constrained by transverse-component full waveform data using the asymptotic coupling technique of *Li and Romanowicz* [1995].

[41] 4. The TXBW [*Grand*, 2002] model is entirely based on shear wave travel times. It is originally parameterized with cells. To facilitate the comparison, we have expanded this model in spherical harmonics up to degree 40.

[42] Some of the model differences are due to differences in the data sets. For example, models based on Love wave phase velocities (e.g., SAW24) yield higher shear velocities at 200 km depth beneath the Pacific Ocean than models based on Rayleigh wave phase velocities (e.g., S20RTS) due to variations in uppermost mantle anisotropy [*Ekström and Dziewonski*, 1998; *Gung et al.*, 2003] that are ignored in the isotropic inversions. Other differences are due to differences in the model parameterizations and inversion strategies. For example, the low velocities just above the 670-km discontinuity beneath continental regions seen in models S20A_SV appears to be an artifact introduced by splitting the parameterization at 670 km depth and by employing vertical smoothness constraints. Despite these differences, the models compare well as is underscored by the relatively high model correlation throughout the transition zone (Figure 13), and the characteristics of S20RTSb that we have highlighted in this paper are common to all of shear velocity models.

[43] **Acknowledgments.** This research has been funded by the NSF grant EAR-0106666. The data used in this study have been provided by the IRIS/DMC and GEOSCOPE. We thank Michael Ritzwoller and Barbara Romanowicz for helpful reviews.

References

Antolik, M., Y. J. Gu, G. Ekstrom, and A. M. Dziewonski (2003), J362D28: A new joint model of compressional and shear velocity in the Earth's mantle, *Geophys. J. Int.*, *153*, 443–466.

Backus, G. E., and J. F. Gilbert (1968), The resolving power of gross earth data, *Geophys. J. R. Astron. Soc.*, *16*, 169–205.

Beucler, E., E. Stutzmann, and J. P. Montagner (2003), Measuring surface-wave higher mode phase velocity measurements using a rollercoaster type algorithm, *Geophys. J. Int.*, *155*, 289–307.

Bolton, H., and G. Masters (2001), Travel time of *P* and *S* from the global digital seismic networks: Implications for the relative variation of *P* and *S* velocity in the mantle, *J. Geophys. Res.*, *106*, 13,527–13,540.

Bonatti, E. (1996), Anomalous opening of the equatorial Atlantic due to an equatorial mantle thermal minimum, *Earth Planet. Sci. Lett.*, *143*, 147–160.

Boschi, L., and A. M. Dziewonski (1999), High and low resolution images of the Earth's mantle: Implications of different approaches to tomographic modeling, *J. Geophys. Res.*, *104*, 25,567–25,594.

Cara, M. (1978), Regional variations of Rayleigh-mode velocities: A spatial filtering method, *Geophys. J. R. Astron. Soc.*, *54*, 439–460.

Cara, M. (1979), Lateral variations of *S*-velocity in the upper mantle from higher Rayleigh modes, *Geophys. J. R. Astron. Soc.*, *57*, 649–670.

Cara, M., and J. J. Lévêque (1987), Waveform inversion using secondary observables, *Geophys. Res. Lett.*, *14*, 1046–1049.

Cizkova, H., O. Cadek, A. P. van den Berg, and N. J. Vlaar (1999), Can lower mantle slab-like seismic anomalies be explained by thermal coupling between the upper and lower mantles?, *Geophys. Res. Lett.*, *26*, 1501–1504.

Debayle, E., and J. J. Lévêque (1997), Upper mantle heterogeneities in the Indian Ocean from waveform inversion, *Geophys. Res. Lett.*, *24*, 245–248.

Deuss, A., and J. H. Woodhouse (2002), A systematic search for mantle discontinuities using *SS*-precursors, *Geophys. Res. Lett.*, *29*(8), 1249, doi:10.1029/2002GL014768.

Dziewonski, A. M., and D. L. Anderson (1981), Preliminary Reference Earth Model, *Phys. Earth Planet. Inter.*, *25*, 297–356.

Ekström, G., and A. M. Dziewonski (1998), The unique anisotropy of the Pacific upper mantle, *Nature*, *394*, 168–172.

Ekström, G., J. Tromp, and E. W. F. Larson (1997), Measurements and global models of surface wave propagation, *J. Geophys. Res.*, *102*, 8137–8157.

Estabrook, C. H., and R. Kind (1996), The nature of the 660-kilometer upper-mantle seismic discontinuity from precursors to the *PP* phase, *Science*, *274*, 1179–1182.

Fukao, Y., M. Obayashi, H. Inoue, and M. Nenbai (1992), Subducting slabs stagnant in the mantle transition zone, *J. Geophys. Res.*, *97*, 4809–4822.

Grand, S. P. (1994), Shear mantle structure beneath the Americas and the surrounding oceans, *J. Geophys. Res.*, *99*, 11,591–11,621.

Grand, S. P. (2002), Mantle shear-wave tomography and the fate of subducted slabs, *Philos. Trans. R. Soc. London, Ser. A*, *360*, 2475–2491.

Gu, Y. J., A. M. Dziewonski, W.-J. Su, and G. Ekström (2001a), Models of the mantle shear velocity and discontinuities in the pattern of lateral heterogeneities, *J. Geophys. Res.*, *106*, 11,169–11,199.

Gu, Y. J., A. M. Dziewonski, and G. Ekström (2001b), Preferential detection of the Lehmann discontinuity beneath continents, *Geophys. Res. Lett.*, *28*, 4655–4658.

Gu, Y. J., A. M. Dziewonski, and G. Ekström (2003), Simultaneous inversion for mantle shear velocity and topography of transition zone discontinuities, *Geophys. J. Int.*, in press.

Gung, Y., M. Panning, and B. Romanowicz (2003), Global anisotropy and the thickness of continents, *Nature*, *422*, 707–711.

Hamilton, W. B. (2002), The closed upper-mantle circulation of plate tectonics, in *Plate Boundary Zones*, *Geodyn. Ser.*, vol. 30, edited by S. Stein and J. T. Freymueller, pp. 359–410, AGU, Washington, D. C.

King, S. D., and J. Ritsema (2000), African hotspot volcanism: Small-scale convection in the upper mantle beneath cratons, *Science*, *290*, 1137–1140.

Laske, G., and G. Masters (1996), Constraints on global phase-velocity maps from long-period polarization data, *J. Geophys. Res.*, *101*, 16,059–16,075.

Lay, T., and H. Kanamori (1985), Geometric effects of global lateral heterogeneity on long-period surface-wave propagation, *J. Geophys. Res.*, *90*, 605–621.

Lerner-Lam, A. L., and T. H. Jordan (1983), Earth structure from fundamental and higher-mode waveform analysis, *Geophys. J. R. Astron. Soc.*, *75*, 759–797.

Lerner-Lam, A. L., and T. H. Jordan (1987), How thick are the continents, *J. Geophys. Res.*, *92*, 14,007–14,026.

Li, X. D., and B. Romanowicz (1995), Comparison of global wave-form inversions with and without considering cross-branch modal coupling, *Geophys. J. Int.*, *121*, 695–709.

Li, X. D., and B. Romanowicz (1996), Global mantle shear velocity model developed using nonlinear asymptotic coupling theory, *J. Geophys. Res.*, *101*, 22,245–22,272.

Masters, G., G. Laske, H. Bolton, and A. Dziewonski (2000), The relative behavior of shear velocity, bulk sound speed, and compressional velocity in the mantle: Implications for chemical and thermal structure, in *Earth's Deep Interior: Mineral Physics and Tomography from the Atomic to the Global Scale*, *Geophys. Monogr. Ser.*, vol. 117, edited by S. Karato et al., pp. 63–87, AGU, Washington, D. C.

Mégnin, C., and B. Romanowicz (2000), The three-dimensional shear velocity structure of the mantle from the inversion of body, surface and higher-mode waveforms, *Geophys. J. Int.*, *143*, 709–728.

Melbourne, T., and D. V. Helmberger (2001), Mantle control of plate boundary deformation, *Geophys. Res. Lett.*, *28*, 4003–4006.

Mitchell, R. G. (1980), Array measurements of higher mode Rayleigh wave dispersion: An approach utilising source parameters, *Geophys. J. R. Astron. Soc.*, *63*, 311–331.

Montagner, J. P. (1998), Where can seismic anisotropy be detected in the Earth's mantle? In boundary layers. . ., *Pure Appl. Geophys.*, *151*, 223–256.

Mooney, W. D., G. Laske, and G. Masters (1998), CRUST5.1: A global crustal model at 5° × 5°, *J. Geophys. Res.*, *103*, 727–747.

Nataf, H.-C., and J. VanDecar (1993), Seismological detection of a mantle plume?, *Nature*, *364*, 115–120.

Ni, S., E. Tan, M. Gurnis, and D. V. Helmberger (2002), Sharp sides to the African superplume, *Science*, *296*, 1850–1852.

Nolet, G. (1975), Higher Rayleigh modes in western Europe, *Geophys. Res. Lett.*, *2*, 60–62.

Nolet, G. (1977), The upper mantle under western Europe inferred from the dispersion of Rayleigh modes, *J. Geophys.*, *43*, 265–285.

Nolet, G. (1990), Partitioned wave-form inversion and 2-dimensional structure under the network of autonomously recording seismographs, *J. Geophys. Res.*, *95*, 8499–8512.

Nolet, G., and F. A. Dahen (2000), Wave front healing and the evolution of seismic delay times, *J. Geophys. Res.*, *105*, 19,043–19,054.

Okal, E. A., and B. G. Jo (1987), Stacking investigations of the dispersion of higher-order mantle Rayleigh-waves and normal-modes, *Phys. Earth Planet. Inter.*, *47*, 188–204.

Pollitz, F. F. (1994), Global tomography from Rayleigh and Love wave-dispersion—Effect of ray-path bending, *Geophys. J. Int.*, *118*, 730–758.

Resovsky, J. S., and M. H. Ritzwoller (1999), A degree 8 mantle shear velocity model from normal mode observations below 3 mHz, *J. Geophys. Res.*, *104*, 993–1014.

Ritsema, J., and H. J. van Heijst (2001), Constraints on the correlation of *P*- and *S*-wave velocity heterogeneity in the mantle from *P*, *PP*, *PPP*, and *PKPab* traveltimes, *Geophys. J. Int.*, *149*, 482–489.

Ritsema, J., S. Ni, D. V. Helmberger, and H. P. Crotwell (1998), Anomalous shear velocity reductions and gradients in the lower mantle beneath Africa, *Geophys. Res. Lett.*, *25*, 4245–4248.

Ritsema, J., H. J. van Heijst, and J. H. Woodhouse (1999), Complex shear velocity structure imaged beneath Africa and Iceland, *Science*, *286*, 1925–1928.

Ritzwoller, M. H., N. M. Shapiro, A. L. Levshin, and G. M. Leahy (2001), Crustal and upper mantle structure beneath Antarctica and surrounding oceans, *J. Geophys. Res.*, *106*, 30,645–30,670.

Robertson, G. S., and J. H. Woodhouse (1995), Evidence for proportionality of *P* and *S* heterogeneity in the lower mantle, *Geophys. J. Int.*, *123*, 85–116.

Shearer, P. M. (1990), Seismic imaging of upper mantle structure with new evidence for a 520-km discontinuity, *Nature*, *344*, 121–126.

Shearer, P. M. (1993), Global mapping of upper mantle reflectors from long-period *SS* precursors, *Geophys. J. Int.*, *115*, 878–904.

Shearer, P. M., and T. G. Masters (1992), Global mapping of topography on the 660-km discontinuity, *Nature*, *355*, 791–796.

Souriau, A., and J. H. Woodhouse (1985), A worldwide comparison of predicted *S*-wave delays from a 3-dimensional upper mantle model with *P*-wave station corrections, *Phys. Earth Planet. Inter.*, *39*, 75–88.

Spakman, W. (1990), Tomographic-images of the upper mantle below central-Europe and the Mediterranean, *Terra Nova*, *2*, 542–553.

Stutzmann, E., and J. P. Montagner (1993), An inverse technique for retrieving higher mode phase-velocity and mantle structure, *Geophys. J. Int.*, *113*, 669–683.

Stutzmann, E., and J. P. Montagner (1994), Tomography of the transition zone from the inversion of higher-mode surface-waves, *Phys. Earth Planet. Inter.*, *86*, 99–115.

Su, W. J., and A. M. Dziewonski (1991), Predominance of long-wavelength heterogeneity in the mantle, *Nature*, *352*, 121–126.

Su, W. J., R. L. Woodward, and A. M. Dziewonski (1994), Degree-12 model of shear velocity heterogeneity in the mantle, *J. Geophys. Res.*, *99*, 6945–6980.

Tanimoto, T. (1990), Long-wavelength *S*-wave velocity structure throughout the mantle, *Geophys. J. Int.*, *100*, 327–336.

Trampert, J., and H. J. van Heijst (2002), Global azimuthal anisotropy in the transition zone, *Science*, *296*, 1297–1299.

Trampert, J., and J. H. Woodhouse (1995), Global phase-velocity maps of Love and Rayleigh-waves between 40 and 150 seconds, *Geophys. J. Int.*, *122*, 675–690.

van der Hilst, R. D., S. Widiyantoro, and E. R. Engdahl (1997), Evidence for deep mantle circulation from global tomography, *Nature*, *386*, 578–584.

van Heijst, H. J., and J. H. Woodhouse (1997), Measuring surface-wave overtone phase velocities using a mode branch stripping technique, *Geophys. J. Int.*, *131*, 209–230.

van Heijst, H. J., and J. H. Woodhouse (1999), Global high-resolution phase velocity distributions of overtone and fundamental-modesurface waves determined by mode branch stripping, *Geophys. J. Int.*, *137*, 601–620.

Vasco, D. W., L. R. Johnson, R. J. Pulliam, and P. S. Earle (1994), Robust inversion of IASP91 travel time residuals for mantle *P* and *S* velocity structure, earthquake mislocations, and station corrections, *J. Geophys. Res.*, *99*, 13,727–13,755.

Wang, Z., J. Tromp, and G. Ekström (1998), Global and regional surface-wave inversions: A spherical-spline parameterization, *Geophys. Res. Lett.*, *25*, 207–210.

Woodhouse, J. H., and A. M. Dziewonski (1984), Mapping the upper mantle: Three-dimensional modeling of earth structure by inversion of seismic waveforms, *J. Geophys. Res.*, *89*, 5953–5986.

Woodhouse, J. H., and A. M. Dziewonski (1986), Three dimensional mantle models based on mantle wave and long period body wave data, *Eos Trans. AGU*, *67*, 307.

Woodhouse, J. H., and Y. K. Wong (1986), Amplitude, phase and path anomalies of mantle waves, *Geophys. J. R. Astron. Soc.*, *87*, 753–773.

Yoshizawa, K., and B. L. N. Kennett (2002), Non-linear waveform inversion for surface waves with a neighbourhood algorithm—Application to multimode dispersion measurements, *Geophys. J. Int.*, *149*, 118–133.

Zhang, Y. S., and T. Lay (1996), Global surface wave phase velocity variations, *J. Geophys. Res.*, *101*, 8415–8436.

J. Ritsema, Département de Sismologie, Institut de Physique du Globe, 4, Place Jussieu Tour 14-24, F-75252 Paris, France. (jeroen@ipgp.jussieu.fr)

H. J. van Heijst, Seismological Laboratory, 252-21, 1200 E. California Blvd., California Institute of Technology, Pasadena, CA 91125, USA. (jeroen@gps.caltech.edu)

J. H. Woodhouse, Department of Earth Sciences, Oxford University, Parks Road, Oxford OX1 3PR, UK.

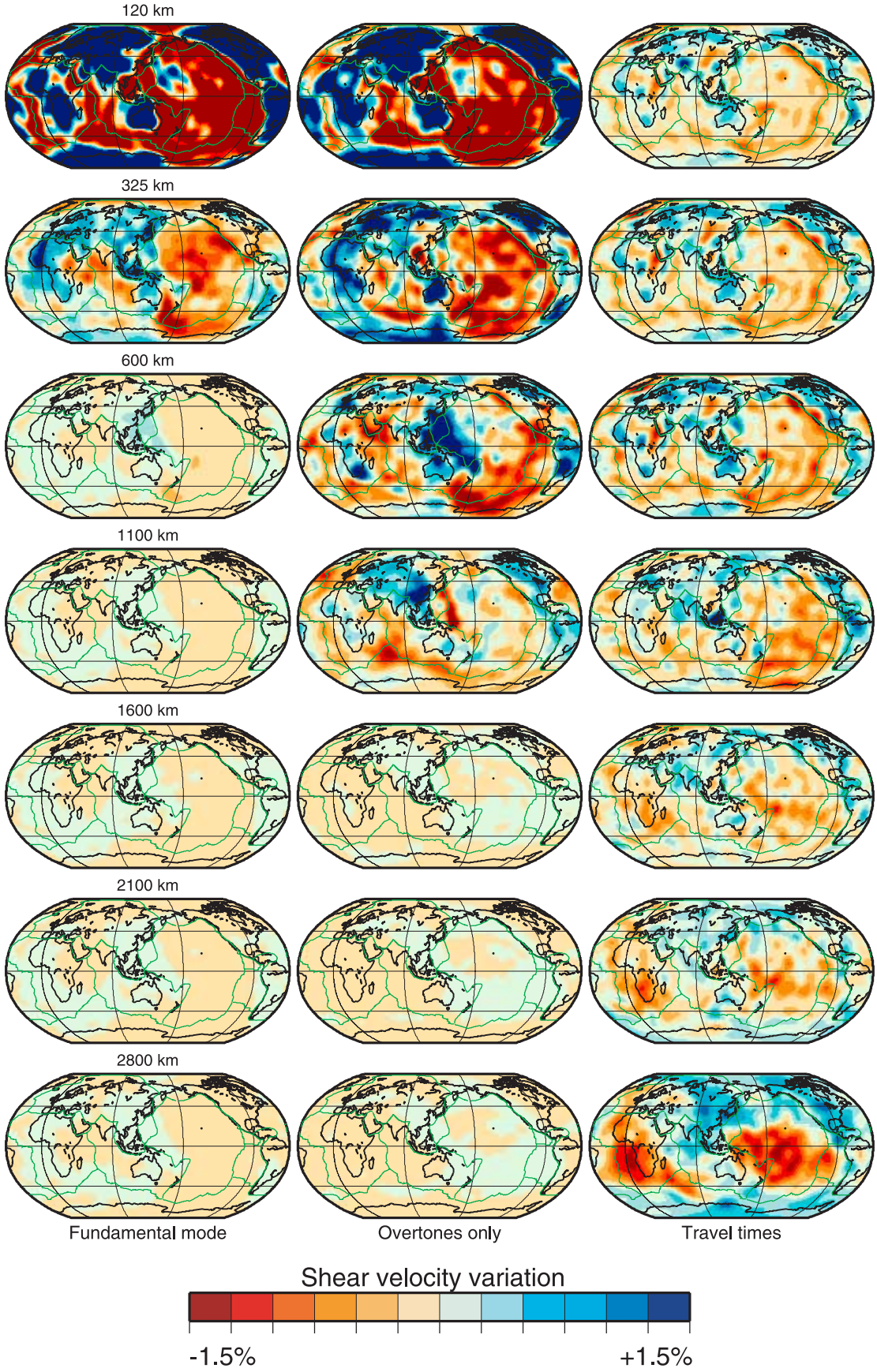
120 km
325 km
600 km
1100 km
1600 km
2100 km
2800 km
Fundamental mode
Overtones only
Travel times
Shear velocity variation
-1.5%
+1.5%

Figure 1.

Figure 1. Models of shear velocity derived by inverting (left) fundamental-mode Rayleigh wave phase velocities (40–200 s), (middle) overtone Rayleigh wave phase velocities, and (right) teleseismic body wave travel times. The color intensity is proportional to the amplitude of the shear velocity perturbation. The color scale ranges from −1.5% to +1.5% to facilitate a comparison of the maps, but actual velocity variations in the uppermost mantle are higher. Velocity heterogeneity can be resolved to at most 400 km depth with fundamental mode Rayleigh wave data, while teleseismic body wave travel times cannot constrain vertical velocity variations in the upper 1000 km of the mantle. Overtone data ideally complement fundamental-mode Rayleigh wave and travel time data for constraining structure in the transition zone.

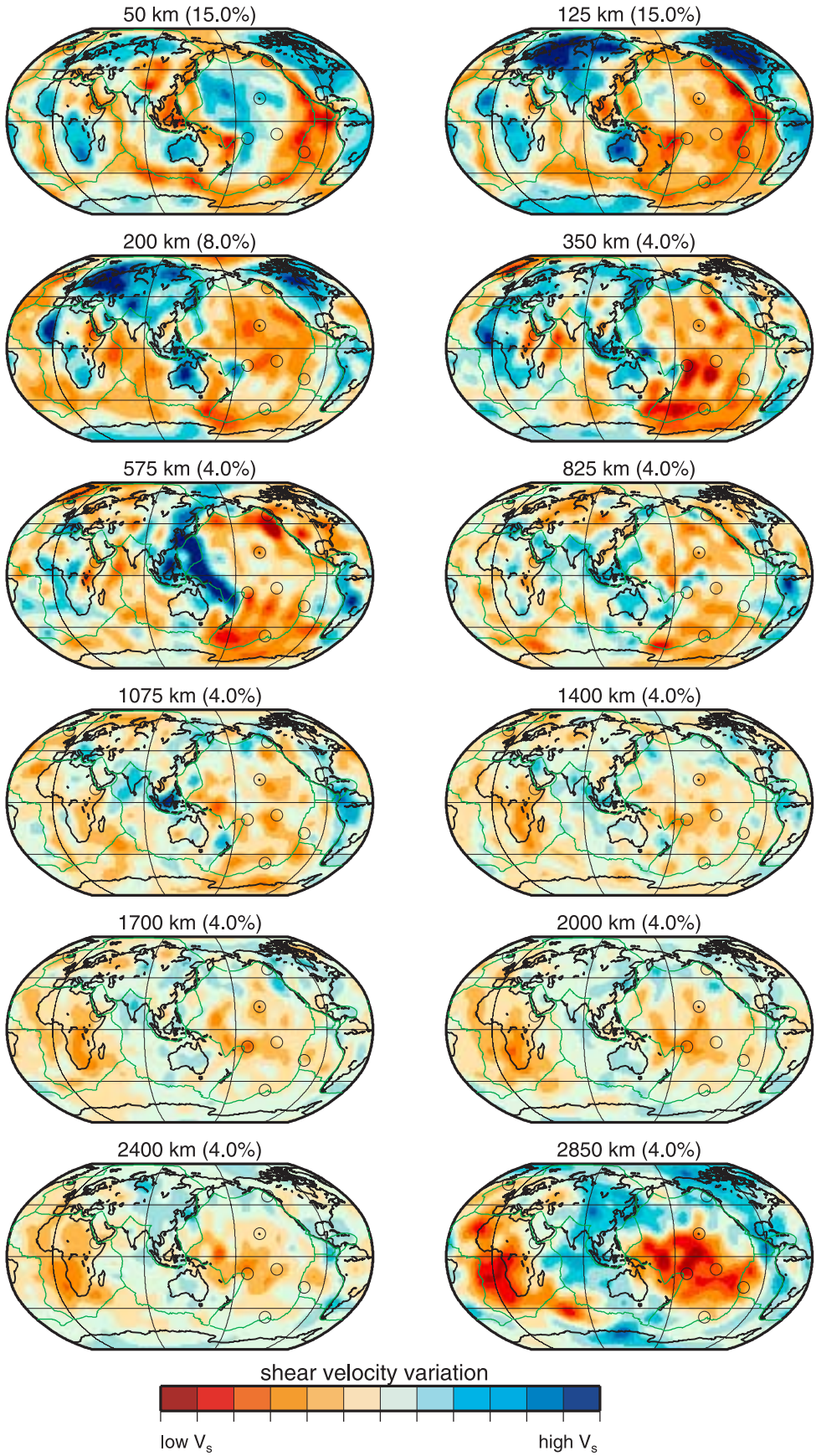
50 km (15.0%)
125 km (15.0%)
200 km (8.0%)
350 km (4.0%)
575 km (4.0%)
825 km (4.0%)
1075 km (4.0%)
1400 km (4.0%)
1700 km (4.0%)
2000 km (4.0%)
2400 km (4.0%)
2850 km (4.0%)
shear velocity variation
low V_s
high V_s

Figure 7.

Figure 7. Maps of shear velocity variation according to model S20RTSb at 50, 125, 200, 325, 575, 825, 1075, 1400, 1700, 2000, 2400, and 2850 km depth. The shear velocity is higher (lower) than the shear velocity in PREM in blue (red) regions. The color intensity is proportional to the amplitude of the shear velocity perturbation. The peak shear velocity perturbation from PREM (in percent) is given above each map. Green lines represent plate boundaries, while the blue circles are at the locations of the Afar, Iceland, Hawaii, Samoa, Tahiti, Easter Island, McDonald, and Bowie hot spots.